



Electric Field Modified Bunsen Flame with Variable Anode Placement

Paulo R. Salvador* and Kunning G. Xu[†]

University of Alabama in Huntsville, Huntsville, Alabama 35899

DOI: 10.2514/1.T5069

A methane–air Bunsen flame was tested under dc electric field forcing with different ring anode sizes and locations. The anodes were placed within the flame to far outside the flame, both axially and radially. The focus of the work is to understand the limit of electrode placement and its effect on the flame under a dc field. A stoichiometric flame with voltages up to 9.1 kV was tested. The electrical current and flame height were measured as a function of the bias voltage and anode location. Plasma density measurements of the unmodified flame at various axial locations were used to corroborate that anode placement at regions of high electron density caused the largest reductions in flame height. The results showed the anodes closest to the burner at 35 mm caused the largest reduction (24%) in flame height. The effect of the electric field on flame height decreased as the anode moved farther downstream of the flame or radially outward. For the same voltage, larger currents were also observed for anodes close to the burner, whereas anodes placed far outside of the flame had minimal effects on current and, consequently, on the flame height. These differences are due to the variable electron density at the anode, which limits the net current collected and the strength of the field.

I. Introduction

THE ability of electric fields to modify flames is well known and has been the subject of research for both premixed and diffusion flames [1–5]. The effect of electric fields on flames has been investigated through experiments and simulations, and the results showed that the field can increase flame blowoff limits at fuel-lean conditions [4,6–8], increased flame burning velocity [3,9,10], decreased emissions and soot formation [11–15], and enhanced flame stability [3,8,16,17]. The possible application of electric fields to control the flame transfer function and thermoacoustic instabilities has also been suggested [18,19]. These various effects have been well documented in the literature; however, results are not always consistent from experiment to experiment, and a unified predictive mechanism is still needed.

A dc electric field can affect flames through three mechanisms: thermal, chemical, and the ionic wind. Thermal heating of the gases is largely ruled out for dc fields due to the very low electrical power consumed, typically less than 1% of the flame's thermal power. Field-induced changes to the chemical kinetics are often debated. The theory is that collisions between neutrals and accelerated electrons and ions promote dissociation of the neutral molecules and dissociative recombination of ions to create radical species such as H and OH that promote combustion. Enhancement of the laminar flame velocity, which is typically a chemical property, in combustion bomb experiments indicates that the field does affect the flame speed and thus chemistry, though the exact process is yet unknown [9,10]. Wisman et al. [20–22] conducted experiments with conical flames and proposed that the electric field causes thermodiffusive instabilities through a combination of changes in the flame chemistry from ion dissociative recombination reactions and reduction of the Lewis number.

The ionic wind is the most accepted mechanism of how external dc electric fields affect flames. The ionic wind is an electro-

hydrodynamic effect resulting from accelerated ions colliding with neutral species in the flame. The ionic wind theory was first proposed by Payne and Weinberg [23] and Lawton and Weinberg [24]. In their experiments, they calculated the maximum current density before electrical breakdown of the air (30 kV/m) to be $j = 0.25 \text{ mA/cm}^2$ and the maximum momentum transfer induced pressure change to be $\Delta p = 0.0004 \text{ atm}$ [24]. Most studies consider the electric field as uniform across the flame and conclude that the flame changes scale with a global electric field or reduce electric field. This neglects the fact that the flame is a weakly ionized plasma where potential and particle distributions are not uniform. Those studies that have considered the existence of the nonuniformity do so mostly in a qualitative manner [22,25,26]. For high-pressure plasma such as flames, the particle density nonuniformity is further enhanced by the high number of collisions that contributes to neutralization reactions.

The objective of the present work is to investigate the impact on the flame response of anode geometry and location close to far away from the flame. With different anode locations, the changing plasma density should change the effect of the field. Section II discusses the experimental setup and image processing code used to determine flame heights. Section III presents the experimental results, and Sec. IV discusses the interaction between the anode locations and the flame.

II. Experimental Setup

The overall experimental setup is shown schematically in Fig. 1. The setup was designed to quantify the flame dynamic response to a bias dc voltage by measuring changes in the flame shape and voltage–current behavior. A commercial Bunsen-type burner 130 mm long and 12 mm i.d. flowing methane and air were used in this experiment. The methane gas was provided from bottled sources, and lab air was supplied by an air compressor. The normal air entrainment slot on the burner was sealed so that the flow rate could be accurately controlled. The flow rates of methane and air were controlled by MKS digital mass flow controllers and kept at constant value of 5.82 l/min at an equivalence ratio of 1.00. A Reynolds number of 643 was calculated for the given burner and flow rate used in the experiment.

A Matsusada Precision (Model AU-10P60) high-voltage power supply provided dc voltages up to 10 kV with the upper electrode positive as the anode and the grounded burner as the cathode. A 1 M Ω high-voltage resistor was placed in between the anode and the power supply to measure the current through the system. The addition of the resistor limited the current flow to a maximum of 10 mA at 10 kV and caused a voltage drop of 9.1% between the power supply and anode. Thus, the actual anode voltage is slightly less than the applied voltage. The actual voltage is reported from here on.

Received 24 August 2016; revision received 26 January 2017; accepted for publication 7 April 2017; published online 19 June 2017. Copyright © 2017 by Paulo R. Salvador and Kunning G. Xu. Published by the American Institute of Aeronautics and Astronautics, Inc., with permission. All requests for copying and permission to reprint should be submitted to CCC at www.copyright.com; employ the ISSN 0887-8722 (print) or 1533-6808 (online) to initiate your request. See also AIAA Rights and Permissions www.aiaa.org/randp.

*Graduate Research Assistant, Department of Mechanical and Aerospace Engineering, Student Member AIAA.

[†]Assistant Professor, Department of Mechanical and Aerospace Engineering, Senior Member AIAA.

Three ring anode geometries were tested during experimentation: small (25 mm o.d., 16 mm i.d.), medium (44 mm o.d., 32 mm i.d.), and large (120 mm o.d., 102 mm i.d.). The small and medium rings were made of steel, and the large ring was made of copper. The different anode materials should have a negligible effect on the results because the secondary electron emission for steel and copper are very similar, especially at the low electron temperatures expected in a flame [27]. Any emitted electrons from the anode should be immediately reabsorbed due to the very high positive voltage of the anode. The ring anodes were placed at axial distances of 35, 50, and 100 mm above the burner exit along centerline.

Figure 2 shows a schematic with the anode axial locations with respective dimensions and an example high-speed image of the flame and small ring anode at 50 mm. The burner was drawn in for scale, and the anode is the glowing horizontal line at the top of the image. The glow is due to heating of the metal. Not all possible combinations of anodes and locations were tested. Table 1 lists the anode configurations tested and the naming scheme used throughout the paper.

A high-speed camera (RedLake MotioPro SI-4) was used to record the flame's response to the electric field for different anode and voltage configurations. The images were captured at 100 frames per second for 3 s with an exposure time of $9997\mu\text{s}$ per frame. The frame rate is not fast enough to capture the high-frequency flame behavior, but this study was primarily interested in the overall average flame response. A slight blurring of the flame edges can be seen in the resulting images due to the exposure time. The high-speed images

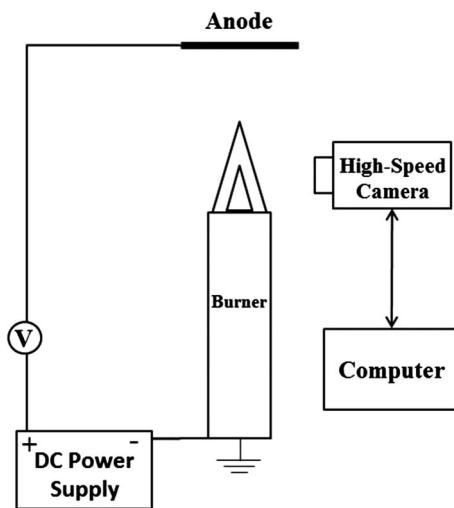


Fig. 1 Experimental setup for flame modification experiment.

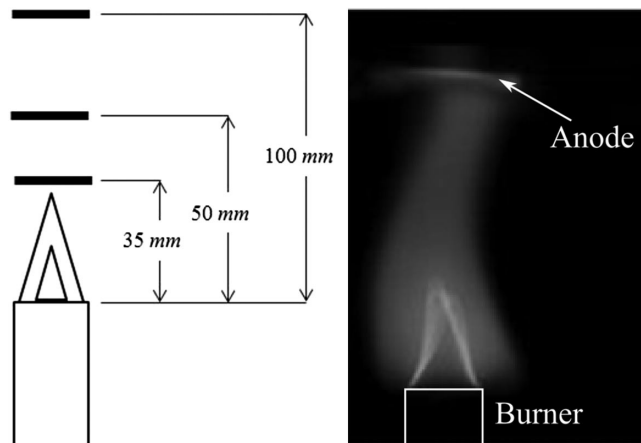


Fig. 2 Anode locations with respective dimensions (left), and an example averaged high-speed image of the flame (right) with the small ring anode at 50 mm (S-50).

Table 1 Anode configurations and labels

Configuration	Ring size	Height, mm
S-35	Small	35
S-50	Small	50
S-100	Small	100
M-35	Medium	35
M-50	Medium	50
L-50	Large	50

were postprocessed using the image processing code developed in Matlab for this study that is described later.

Two-dimensional (2-D) numerical simulations were performed in finite element method magnetics (FEMM) to predict the electric field distribution generated by the various high-voltage electrode configurations. The simulations were performed with a grounded burner and positively charged ring electrodes up to 10 kV. No flame was simulated because the software used was not able to account for nonair mediums.

A Matlab code was developed to analyze the high-speed images to determine the flame height. The experiment sought to use changes in the flame height to quantify the effect of the field. The code has three main parts: averaging high-speed images, flame front segmentation, and conversion from pixel to units of length. The code developed for this study provides a systematic and consistent method of calculating the flame height.

The first part of the code created an averaged image from a specific number of high-speed frames. A desired number of n images for one anode configuration and electric field strength were inputted and summed together in Matlab to create a single superimposed image. The summation is performed by adding pixel by pixel from all n images. The superimposed image is divided by n to create a final averaged image. The averaged image is then processed by applying filters to determine the pixel gradient magnitude, reduce noise, and create a sharper image. The watershed transform function is used to directly segment regions where high pixel gradient magnitudes are found. The transform finds ridge lines in an image where low-level pixels are treated as higher elevations, and high-level pixels are treated as lower elevations. This function creates a mask that highlights the high gradient pixels, that is, the flame front, allowing for easier identification of its edges. The last part of the code creates a tool that measures the number of pixels between two points in the image. The two points are selected at the flame tip and burner, which composes the flame height. The point selections are easily performed with the assistance from the watershed mask previously applied to the flame front. The number of pixels in between the two points are then converted into millimeters and displayed to the user. The process is repeated for all data sets with different anode configurations and electric field strengths. Figure 3 summarizes and shows images of this process.

III. Results

A. Electrical Characteristics

The centerline anode voltage and resulting current drawn through the flame are shown in Fig. 4 for the different anodes. The data are plotted as a function of voltage as opposed to a global electric field defined as the voltage divided by the electrode separation because the actual electric field within the flame is not constant and will vary depending on the charged particle density and thickness of the burner plasma sheaths [22,25,28,29]. The plot shows that current has the same profile for a given location for both small and medium anode rings. The small ring tended to draw more current for a given voltage, likely due to the larger fraction of the ring area directly exposed to the flame. The small and medium anodes all have exponential current profiles, which indicate an asymptotic upper limit on the current, which means an upper limit on the effect of the electric field on the flame, without gas breakdown. The cause for this upper limit is usually current saturation of the cathode as seen and described by other works [16,29–32]. At high enough voltages, all ions produced

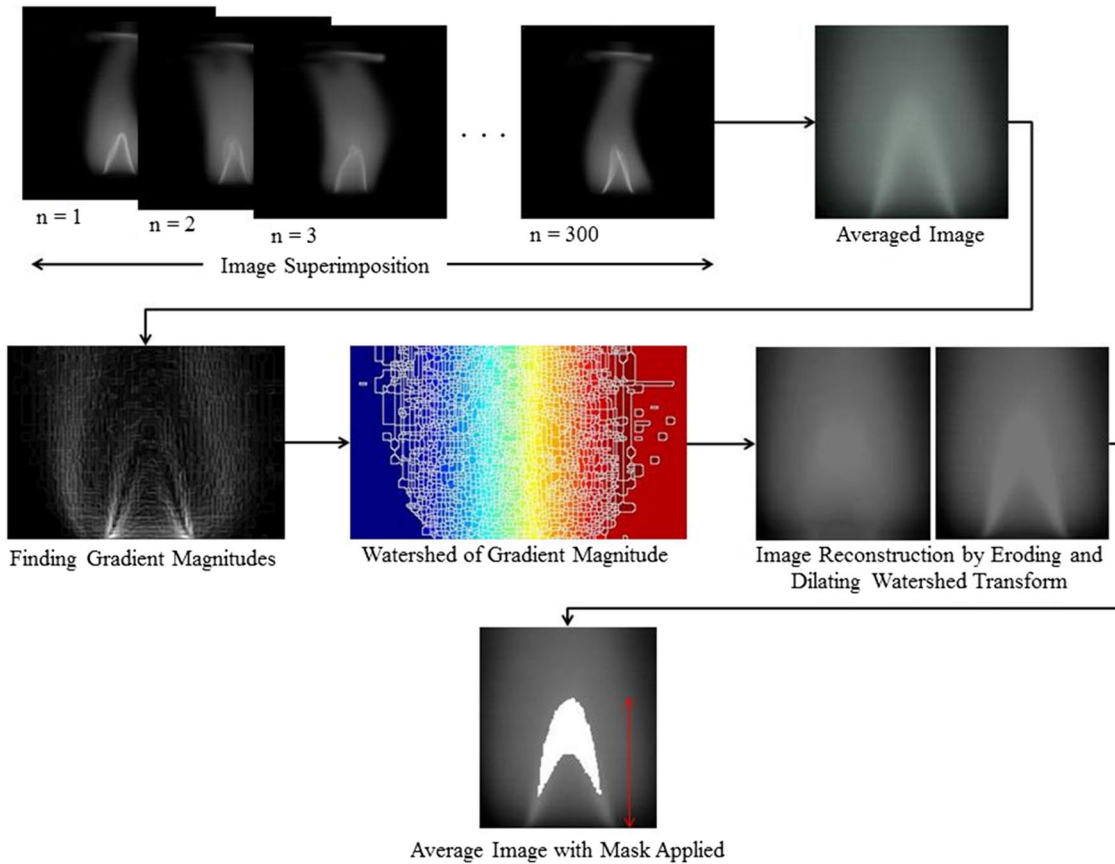


Fig. 3 Matlab code process to find the flame front edges and facilitate flame height measurements.

in the flame front are attracted to the cathode and collected, thereby preventing further increase in current flux. Jacobs and Xu confirmed this behavior with ion density measurements inside a quasi-one-dimensional flame under a dc electric field [30]. They found that the increase in ion density plateaued at 6 kV, and further increase in voltage caused no change in the ion density and current.

From Fig. 4, it is clear that, at 50 mm, both small and medium rings have a higher saturation current as well as a slower current growth than their 35 mm counterparts. In contrast to the small and medium rings, the large ring at 50 mm drew a much lower current and with nearly a linear profile. Because the flame and voltages are the same for all cases, the differences are due to the location and size of the anode. Anode location affects the global electric field strength, but the scaling is not clear. The location also affects the density of charged particles present, specifically electrons. In order for the electrical circuit to draw a current through the flame, there must be net ions at the cathode and net electrons at the anode. For every ion collected by the cathode (burner), an electron must be collected by the anode. Ion and electron formation occurs just downstream of the

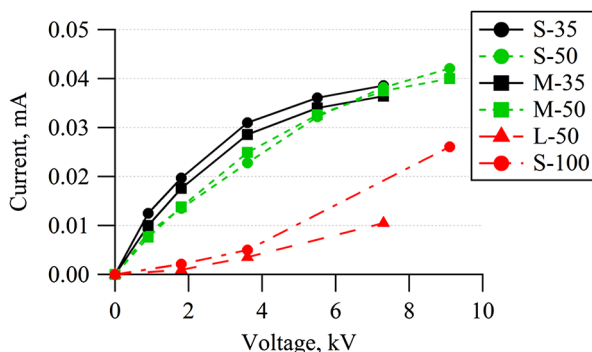


Fig. 4 Current/voltage characteristic curves for the centerline anodes.

flame front due to the primary reaction requiring H_2O , which is formed mainly in the burned gas. As shown in Fig. 2, the 50 mm anode is near the tip of the outer burned gas cone, whereas the 35 mm anode would be closer to the flame front. Thus, the 35 mm anode would see a higher density of charged particles, resulting in increased electron density compared to the 50 mm anode. This causes a higher current to be drawn at a given voltage, as seen in Fig. 4. The 50 mm case has a higher limit, however, because of the additional gas volume that is not seen by the 35 mm anode. Simply, the higher anode has a lower local density but can collect electrons from the entire flame gases, resulting in a total higher current.

The large ring is, however, located well outside the flame. As shown by Goodings et al. [33] and Prager et al. [34], the concentration of flame ions and electrons falls off rapidly outside of the flame front, assuming no external ionization source. Thus, electron density at the large anode is much smaller compared to the ion density at the burner. The current drawn through the electrical circuit is now strongly limited by the presence of electrons at the anode. The 100 mm small anode case (S-100) shows a similar low-current profile as the large ring due to its distance from the flame and thus low electron densities. The tip of the burned gas cone is at or just below 50 mm. Thus, at 100 mm above the burner, the small anode is also well outside of the flame. The electron density for S-100 is larger than L-50 due to the different particle transport mechanisms. The S-100 anode sits above the flame and sees charged particles primarily due to convection from the burned gas flow. In contrast, the L-50 anode mainly sees charged particles from much slower radial diffusion. Because ions and electrons are lost primarily through recombination reactions with each other, the higher convective flow velocity will reduce the amount of particles lost to recombination. This results in a higher density for the S-100-0 case and thus a higher possible electrical current.

Electrons at the anode are emphasized here because the cathode generally sees the same flame independent of the anode location. Thus, the ion density and current should be consistent across the

different cases. It is then the electrons at the anode that limit the current draw possible for anodes located outside of the flame.

B. Flame Structure

High-speed images were captured to analyze the average flame response and structure to the external electric field. Example images of the flame under a 0 and 9.1 kV electric field are shown in Fig. 5 for the S-50 configuration. The images cover a 100 ms time span, except for the 9.1 kV case, which covers a 200 ms time span, with individual image exposure times of 9997 μ s.

At 0 kV, the flame has a relatively stable shape with a conical premixed flame and symmetric burned gas cone. The small oscillations in the premixed flame cone are due to motion of the ambient air. A regular shedding motion of the burned gas can be seen, caused by heating and rising of the air around the flame and entrainment of cooler air from under the flame. With a 9.1 kV electric field applied, the premixed flame front shrinks and shows large oscillations and periods of collapse and wrinkling at 20–30 ms. The flame front recovers at 50 ms but repeats this collapsing behavior with a \sim 100 ms cycle time. The recovery is due to the convection of fresh gas from the burner. The maximum flow speed is 85 cm/s based on the metered flow rate and burner diameter. For a 25-mm-tall premixed flame, the time for fresh flow to reach the tip is 29 ms. From Fig. 5, the recovery time from the collapsed state is approximately 25 ms, very similar to the flow time.

Similar intermittent collapse and wrinkling of the premixed were also observed by Wisman et al. with a steady dc field [22] as well as with pulsed dc fields [16,35]. These types of flame structure changes are typically attributed to the ionic wind, a dynamic pressure from the collision of energized positive ions with neutrals in the flame and upstream reactants. The externally applied electric field energizes the ions and generates an electric pressure on the flame front and is able to modify the flame front by causing it to collapse inward toward the flame axis. Ganguly and Schmidt used an offset wire anode with a 2.7 kV pulsed dc signal and showed creation of a local zone of flame wrinkling and compression that originates at the burner and propagates upward with the flow [36].

A flame should naturally resist a collapsed state and attempt to return to a conical equilibrium shape, unless the perturbation is continually applied. With pulsed voltage, the continual collapse of the flame front is due to a continuous train of ionic wind body forces or perturbations that push down on the flame. At sufficiently high frequencies and voltages, the pulses can prevent the flow from

equilibrating. This suggests that the collapse phenomenon is related to a fast rising electric field. With a steady dc field, however, after the initial slow voltage rise, the flame should find a new stable structure and resist collapse. However, as seen here and in Wisman et al.'s work [22], a steady field can cause flame collapse, though intermittently. This indicates a departure from a stable equilibrium, which can be attributed to external flow disturbances. In that work as well as here, the flame is not shielded with a coflow; thus, disturbances from the ambient air are present. Normally, those disturbances are not sufficient to significantly alter the flame structure, as evident in the 0 kV images in Fig. 5. Thus, we can conclude that the steady dc field increases the flame's sensitivity to small disturbances to the point of flame collapse.

In addition to collapsing the premixed flame front, the dc field also reduces the maximum height of the stable premixed flame. Figure 6 shows a side-by-side comparison of 0 and 9.1 kV flames at their maximum heights for the S-50 configuration. All images were taken with the camera and burner at the same position. There is a clear reduction in flame height with the applied field. At the same time, the flame root attachment point at the burner appears to move down slightly. The electric field has both a steady forcing effect on the flame that decreases the flame height and a time-dependent effect that collapses the flame front.

The changes to the premixed flame are difficult to see without the aid of high-speed imaging; however, the burned gas region exhibited clear changes to the naked eye with increased voltage. Figure 7 shows the averaged high-speed images for the S-35 case. The burned gas experiences a downward push, outward growth, and a significant increase in the amplitude of oscillations. The radial expansion of this region indicates that the ions in the postflame are being pushed farther away from the centerline, especially near the burner exit, which occurs if the burner exit axial velocity is reduced and radial velocity is increased. Similar results have been obtained by other researchers with particle image velocimetry imaging that show a decrease in the axial velocity and increase in radial velocity at the root of the flame [35,37]. Because the metered flow rate was constant, the flow through the burner was constant. However, the exiting flow can change. The electric field causes ion momentum transfer collisions with the exiting unburned reactants to produce an adverse force or pressure that slows the exit flow velocity and radially spreads out the velocity profile.

To quantify the flame height changes of the premixed flame, the Matlab image processing code discussed previously was used to conduct a systematic analysis of the different anode configurations. The average flame heights for the centerline anodes are shown in

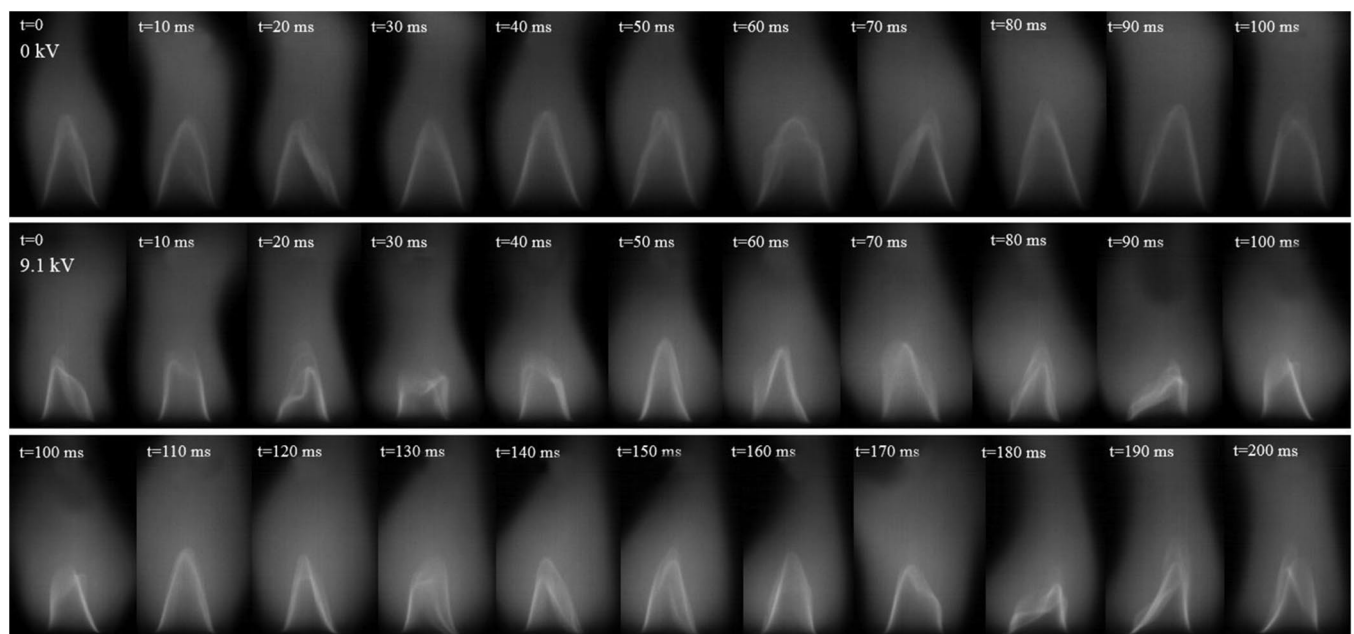


Fig. 5 Images of the flame for the S-50 case at 0 kV (top) and 9.1 kV (middle and bottom).

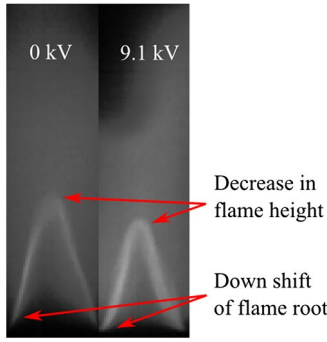


Fig. 6 Comparison of single frame max height flame for 0 kV (left) and 9.1 kV (right).

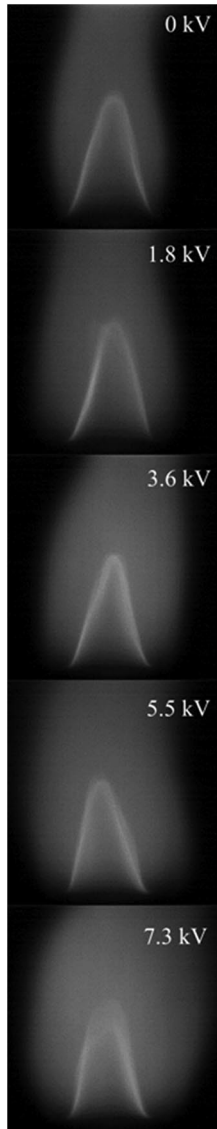


Fig. 7 Expanding diffusion flame for S-35 case.

Fig. 8. The plot shows the flame height normalized by the maximum value, which in most cases was at 0 kV. The 0 kV premixed flame height was ~25 mm. Small variations in the height are due to inherent uncertainties of the burner and flow controller for day-to-day operation. Table 2 provides the percent random error in the measurements of flame height based on a 95% confidence interval using the *t*-distribution analysis. It should be noted that the flame height was calculated from a composite of 300 images; thus, there is an uncertainty contribution due to the oscillations of the flame and a contribution from the frames of the collapsed flame. However, the

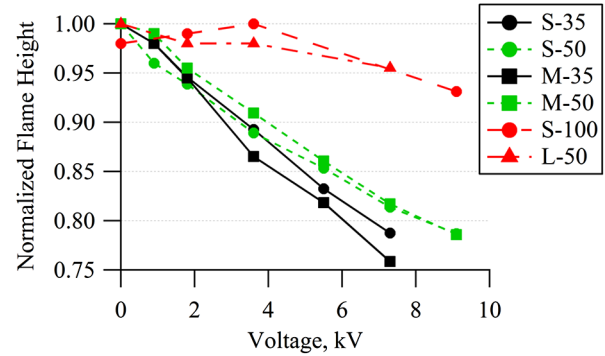


Fig. 8 Normalized flame height for the centerline anode configurations.

collapsed flame occurred less than 5% of the observation time, and as Fig. 6 shows, there is a clear decrease in flame height with the electric field.

Similar to the current–voltage characteristics, both the 35 and 50 mm anodes decrease the flame height, with the 50 mm anodes having a smaller effect. The small and medium anodes also exhibit a similar level of effect at a given location. It can be concluded that the size and shape of the anode is less important than the location, assuming that the anode is small enough to be in full contact with the flame plasma.

The distant anodes, S-100 and L-50, have a much smaller effect on the flame height, just as they drew a much smaller electrical current. Visually, they caused much fewer oscillations in the premixed flame, with no collapses of the flame front. The cause of the reduced effect on flame height is the physical distance between the flame and the anode. For electrical current, the large separation reduced the density of electrons at the anode, thus limiting the possible current. For flame height, which is normally related to a global electric field ($E = V/d$) or the reduced electric field (E/n), the larger distance reduces the global electric field strength. However, the field strength does not appear to be the only factor. Consider the S-50-0 and S-100-0 cases, the latter is twice the distance and thus has half the electric field strength for a given voltage. If the flame height change is a directly function of just field strength, one would expect the 100 mm anode to produce the same reduction in flame height at double the voltage. But as shown, the same 94% flame height is obtained at only 1.8 kV for 50 mm, but 9.1 kV for 100 mm, a five times increase in voltage for the same effect. This indicates that there are other factors involved other than just a global electric field strength.

The flame height results match the current results very well in terms of a higher current producing a larger reduction in flame height. This indicates a linkage between the current to the electrodes and the resulting ionic wind force, which other authors have mentioned as well in terms of a cathode saturation current [13,16,29,32,37,38]. However, here we see the cathode ion density is not always the limiter or the first to saturate. For anodes not directly inside the flame, the electron density (and thus anode current) becomes the limiting factor on the effect of a subbreakdown electric field.

C. Numerical Simulations

Table 3 compares numerical simulations performed in FEMM of the different anode configurations. The side-by-side comparisons

Table 2 Uncertainty all anode configurations and operating conditions tested

Bias voltage, kV	S-35	S-50	M-35	M-50	S-100	L-50
0	18.2	12.2	18.8	10.1	1.8	4.8
1	9.9	13.6	11.9	13.2	—	—
2	7.5	13.2	8.9	19.1	2.0	1.8
4	6.6	10.0	4.8	13.9	5.3	1.1
6	3.9	13.0	7.1	16.5	—	—
8	10.9	12.0	6.2	16.2	—	—
10	—	13.4	—	15.1	1.3	3.4

Table 3 Electric field model for different ring anode sizes and locations

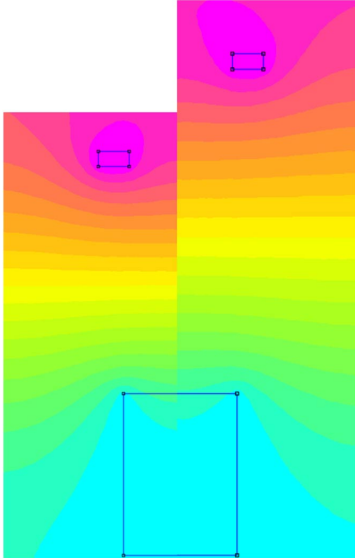
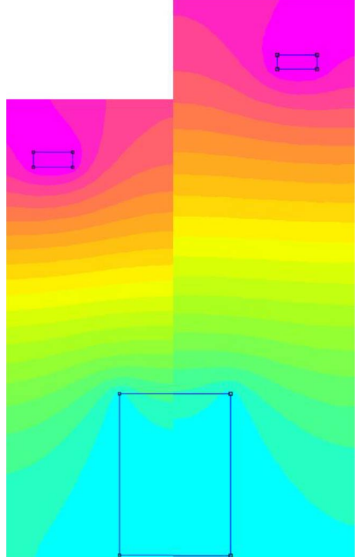
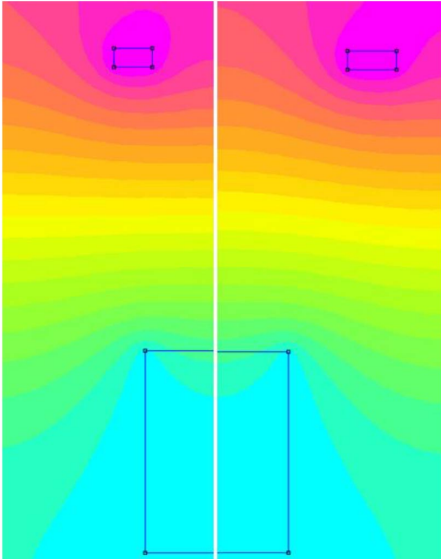

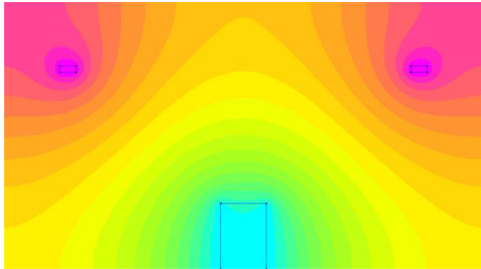
Burner/anode configuration	Model	$E, V/m$																																								
S-35 (left) and S-50 (right)		<table border="1"> <tr><td>8.550e+003</td><td>: >9.000e+003</td></tr> <tr><td>8.100e+003</td><td>: 8.550e+003</td></tr> <tr><td>7.650e+003</td><td>: 8.100e+003</td></tr> <tr><td>7.200e+003</td><td>: 7.650e+003</td></tr> <tr><td>6.750e+003</td><td>: 7.200e+003</td></tr> <tr><td>6.300e+003</td><td>: 6.750e+003</td></tr> <tr><td>5.850e+003</td><td>: 6.300e+003</td></tr> <tr><td>5.400e+003</td><td>: 5.850e+003</td></tr> <tr><td>4.950e+003</td><td>: 5.400e+003</td></tr> <tr><td>4.500e+003</td><td>: 4.950e+003</td></tr> <tr><td>4.050e+003</td><td>: 4.500e+003</td></tr> <tr><td>3.600e+003</td><td>: 4.050e+003</td></tr> <tr><td>3.150e+003</td><td>: 3.600e+003</td></tr> <tr><td>2.700e+003</td><td>: 3.150e+003</td></tr> <tr><td>2.250e+003</td><td>: 2.700e+003</td></tr> <tr><td>1.800e+003</td><td>: 2.250e+003</td></tr> <tr><td>1.350e+003</td><td>: 1.800e+003</td></tr> <tr><td>9.000e+002</td><td>: 1.350e+003</td></tr> <tr><td>4.500e+002</td><td>: 9.000e+002</td></tr> <tr><td><0.000e+000</td><td>: 4.500e+002</td></tr> </table> <p>Density Plot: V, Volts</p>	8.550e+003	: >9.000e+003	8.100e+003	: 8.550e+003	7.650e+003	: 8.100e+003	7.200e+003	: 7.650e+003	6.750e+003	: 7.200e+003	6.300e+003	: 6.750e+003	5.850e+003	: 6.300e+003	5.400e+003	: 5.850e+003	4.950e+003	: 5.400e+003	4.500e+003	: 4.950e+003	4.050e+003	: 4.500e+003	3.600e+003	: 4.050e+003	3.150e+003	: 3.600e+003	2.700e+003	: 3.150e+003	2.250e+003	: 2.700e+003	1.800e+003	: 2.250e+003	1.350e+003	: 1.800e+003	9.000e+002	: 1.350e+003	4.500e+002	: 9.000e+002	<0.000e+000	: 4.500e+002
8.550e+003	: >9.000e+003																																									
8.100e+003	: 8.550e+003																																									
7.650e+003	: 8.100e+003																																									
7.200e+003	: 7.650e+003																																									
6.750e+003	: 7.200e+003																																									
6.300e+003	: 6.750e+003																																									
5.850e+003	: 6.300e+003																																									
5.400e+003	: 5.850e+003																																									
4.950e+003	: 5.400e+003																																									
4.500e+003	: 4.950e+003																																									
4.050e+003	: 4.500e+003																																									
3.600e+003	: 4.050e+003																																									
3.150e+003	: 3.600e+003																																									
2.700e+003	: 3.150e+003																																									
2.250e+003	: 2.700e+003																																									
1.800e+003	: 2.250e+003																																									
1.350e+003	: 1.800e+003																																									
9.000e+002	: 1.350e+003																																									
4.500e+002	: 9.000e+002																																									
<0.000e+000	: 4.500e+002																																									
M-35 (left) and M-50 (right)																																										
S-35 (left) and M-35 (right)																																										

Table 3 (Continued.)

Burner/anode configuration	Model	$E, V/m$
S-100		
L-50		

show how the electric field potential distribution, represented by the contour plots, differs between configurations. For a given anode size, reducing the distance between the electrodes compresses the potential contours and increases the magnitude of the electric field along the burner centerline, which results in a stronger effect on the flame structure. A comparison between the models show that the S-35 and M-35 cases have a larger potential gradient than their 50 mm counterparts, which indicates that these electrode configurations will cause the flame height to be the smallest. This matches the flame height results shown in Fig. 8. The small anodes also exhibited a bump in the centerline electric field compared to the medium anodes at both 35 and 50 mm. This bump is due to the size of the small anode that creates a more uniform field close to the anode. This is clearly seen in Table 3, which compares the S-35 and M-35 simulations. The plot shows that, close to the burner, the potential contours are very similar between the two cases. However, farther downstream and especially around the anode, the M-35 contours are larger, which results in lower electric field strengths. It is likely that a fully closed potential contour such as provided by a plate or fine mesh anode would have an even larger electric field, but those shapes present practical difficulties for actual engine use.

The simulations also confirm the minimal effect that the S-100 and L-50 cases have in the flame height reduction due to low potential gradient, characterized by the small electric field magnitude. Figure 9 plots the centerline electric field magnitude for the different anode configurations as a function of the distance between the anode and cathode. From the figure, it is evident that the S-35 and M-35 cases generate the strongest electric field, followed by the 50 mm cases. Although weak, the S-100 case produced the most uniform electric field magnitude along the entire centerline.

IV. Discussion

A. Electrical Power Consumption

The flame height as a function of the electrical power is shown in Fig. 10. Power serves as a better comparison than either voltage or global electric field here because of the different anode distances. In general, the power results agree with the voltage plot, showing that the closer anodes have a larger effect. Figure 8 does highlight the M-35 case as having the largest reduction in flame height. This may be due to the medium anode having a larger surface area than the small anode, thereby resulting in more field lines and a larger ionic wind area. At 50 mm, the anode is above the flame entirely and thus can “see” a greater volume of flame and perturbations. If the change in flame height is taken as an indicator of other flame properties such as blowoff

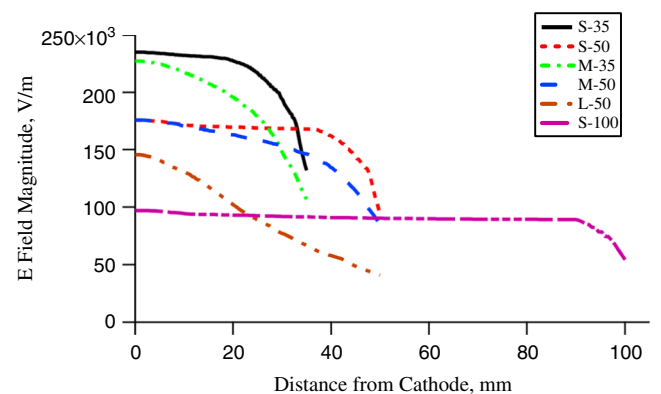


Fig. 9 Electric field magnitude along the burner centerline as a function of electrode gap.

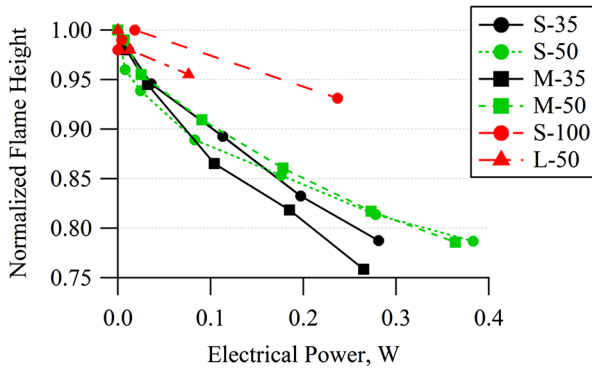


Fig. 10 Normalized flame height as a function of electric power through the power supply.

velocity and stability, then the most efficient geometry is the M-35 anode, except at low voltages, where the S-50 anode is more efficient. This is likely due to the more concentrated electric field generated by the smaller anode being more effective at low field strengths.

B. Anode Location and Electron Density

The results in this work clearly show that anode location plays a strong role in the flame response. This agrees with the results of Gan et al. [31] but disagrees with the results of Wisman et al. [22]. Both showed changes in electrical current with different anode locations, but whereas Gan saw changes in the blowoff limit with location, Wisman saw no changes in flame shape. There are fuel differences between the works; however, the main experimental difference between this and previous works, and the goal of this study, was the location of the anode inside and far outside of the flame. Gan's anode was always outside of the flame, whereas Wisman's anode was always inside the flame. Thus, the electron density around the anodes changed little.

A spatially varying electron density at the different anode locations is the likely cause of the deviation from a pure global electric field scaling, as shown by the differences between the S-50-0 and S-100-0 cases. If the flame had a uniform plasma density everywhere, then the same field strength at different distances should produce the same results. The plasma density along centerline for the 0 kV flame has been measured using single Langmuir probes following the method used by Jacobs and Xu [30]. Briefly, a 2-mm-long, 0.13-mm-diam tungsten filament protruding from a 1.6-mm-diam alumina tube was inserted into the flame. The probe voltage was varied with a source meter, and the resulting current to the filament was measured. The ion density was calculated using the measured ion saturation current at -5 V using the equations for Langmuir probes in high-pressure plasmas [30,39]. The total duration of the probe exposure was kept under 6 s to limit carbon deposition.

We will assume that quasi neutrality exists everywhere except near the electrodes; thus, the electron density is taken equal to the measured plasma density. The results are shown in Fig. 11 from 0 to 50 mm, where zero is just above the exit plane of the burner. Measurements above 50 mm were not obtained due to limitations in the probe traverse system. For reference, the premixed tip is around 25 mm. The measurements show that the plasma density continually increases from the burner exit and reaches a peak just downstream of the premixed flame. The peak around 30–35 mm is due to the large presence of H_3O^+ ions that are formed predominately in the postflame products from reaction between H_2O and CHO^+ [33,34,40]. The gradual increase from 0 to 30 mm is due to backward mass diffusion from the premixed flame. After the peak, there is a decrease in density due to neutralization recombination between the premixed flame ions and electrons. However, the density begins to rise again at 45 mm. The cause of this is likely due to additional ion production reactions in the burned gas. Above 50 mm, there will be a second peak in ion density before the density begins to drop off as ion and electron neutralization begin to dominate.

The anode location of 35 or 50 mm will affect the available electron density and thus current through the system. As shown in Fig. 4, the

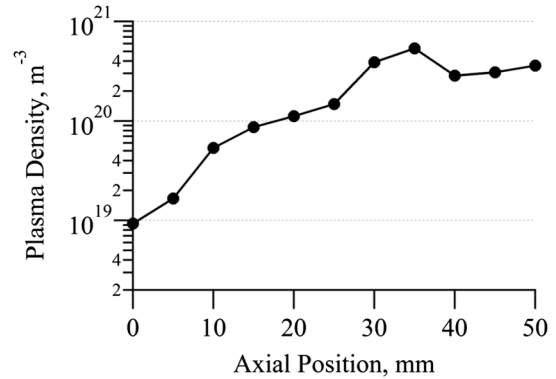


Fig. 11 Plasma density measured along centerline in the 0 kV flame.

S-50 and M-50 anodes had generally a lower current than their 35 mm counterparts until about 7.3 kV. With increasing voltage, the premixed flame and burned gas region heights are reduced, as seen in Figs. 7 and 8. This height reduction shifts the plasma density curve upstream, or leftward in Fig. 9, and thus places the second peak closer to the 50 mm anode. The 50 mm anodes now see both high-density peaks, resulting in a higher possible current. For the S-100 anode, one can imagine that the plasma density will be significantly lower at that height, and thus a very limited electron current can be drawn, which limits the effect of the electric field. A similar situation exists for the L-50 anode. With the electric field, the plasma density distribution will change due to changes in flame shape as well as electrostatic forces. However, because the ion and electron sources are highly localized at the flame front, the general profile should remain the same. Measurements in a field-modified flame were not taken, however.

V. Conclusions

In this study, changes to the flame structure with different sizes and position anodes were investigated. It was shown that the plasma density at the electrodes, and specifically the anode in this work, controls the electrical current and thus the level of flame forcing possible. This means that a conductive path with highly charged particle densities between the electrodes is necessary for the dc electric field to have an effect, without causing air breakdown. Changes in the flame were most significant for anodes closer to the cathode, though the 50 mm anodes had larger effects at higher voltage when the flame was significantly reduced. Negligible changes to the flame were observed with anodes placed a significant distance either radially or axially from the cathode. The low density of electrons at these locations limits the conductive path between the electrodes and reduces the current possible, which in turn reduces the density of accelerated ions and the ionic wind force. The ionic wind is the most likely cause of the observed changes with different anode locations. The result indicates that the optimal design of a practical system needs to consider not only the power source but also the size and location of the electrodes with respect to the plasma density distribution in the system. A 2-D map of the flame plasma density at different voltages is needed for better insight into the interactions between the electric field and flame.

Acknowledgments

This work was supported by the University of Alabama in Huntsville. The authors would like to thank the Propulsion Research Center staff for support as well as fellow students for assistance with the experiment and testing.

References

- [1] Bradley, D., and Weinberg, F. J., *Advanced Combustion Methods*, Academic Press, London, 1986, p. 331.
- [2] Bradley, D., and Nasser, S. H., "Electrical Coronas and Burner Flame Stability," *Combustion and Flame*, Vol. 55, No. 1, 1984, pp. 53–58. doi:10.1016/0010-2180(84)90148-2

- [3] Jagers, H. C., and von Engel, A., "The Effect of Electric Fields on the Burning Velocity of Various Flames," *Combustion and Flame*, Vol. 16, No. 3, 1971, pp. 275–285.
doi:10.1016/S0010-2180(71)80098-6
- [4] Calcote, H. F., and Pease, R. N., "Electrical Properties of Flames: Burner Flames in Longitudinal Electric Fields," *Symposium on Combustion and Flame, and Explosion Phenomena*, Vol. 3, No. 1, 1948, pp. 245–253.
doi:10.1016/S1062-2896(49)80033-X
- [5] Calcote, H. F., and Berman, C. H., "Increased Methane-Air Stability Limits by a DC Electric Field," *Proceeding of the ASME Fossil Fuels Combustion Symposium*, American Soc. of Mechanical Engineers, New York, 1989, pp. 25–31.
- [6] Bak, M. S., Im, S. K., Mungal, M. G., and Cappelli, M. A., "Studies on the Stability Limit Extension of Premixed and Jet Diffusion Flames of Methane, Ethane, and Propane Using Nanosecond Repetitive Pulsed Discharge Plasmas," *Combustion and Flame*, Vol. 160, No. 11, 2013, pp. 2396–2403.
doi:10.1016/j.combustflame.2013.05.023
- [7] Belhi, M., Domingo, P., and Vervisch, P., "Direct Numerical Simulation of the Effect of an Electric Field on Flame Stability," *Combustion and Flame*, Vol. 157, No. 12, 2010, pp. 2286–2297.
doi:10.1016/j.combustflame.2010.07.007
- [8] Ata, A., Cowart, J. S., Vranos, A., and Cetegen, B. M., "Effects of Direct Current Electric Field on the Blowoff Characteristics of Bluff-Body Stabilized Conical Premixed Flames," *Combustion Science and Technology*, Vol. 177, No. 7, 2005, pp. 1291–1304.
doi:10.1080/0010220059050476
- [9] Duan, H., Wu, X., Sun, T., Liu, B., Fang, J., Li, C., and Gao, Z., "Effects of Electric Field Intensity and Distribution on Flame Propagation Speed of CH₄/O₂/N₂ Flames," *Fuel*, Vol. 158, Oct. 2015, pp. 807–815.
doi:10.1016/j.fuel.2015.05.065
- [10] Meng, X., Wu, X., Kang, C., Tang, A., and Gao, Z., "Effects of Direct-Current (DC) Electric Fields on Flame Propagation and Combustion Characteristics of Premixed CH₄/O₂/N₂ Flames," *Energy & Fuels*, Vol. 26, No. 11, 2012, pp. 6612–6620.
doi:10.1021/ef201465w
- [11] Kono, M., Carleton, F. B., Jones, A. R., and Weinberg, F. J., "The Effect of Nonsteady Electric Fields on Sooting Flames," *Combustion and Flame*, Vol. 78, Nos. 3–4, 1989, pp. 357–364.
doi:10.1016/0010-2180(89)90023-0
- [12] Saito, M., Sato, M., and Sawada, K., "Variation of Flame Shape and Soot Emission by Applying Electric Field," *Journal of Electrostatics*, Vol. 39, No. 4, 1997, pp. 305–311.
doi:10.1016/S0304-3886(97)00127-7
- [13] Sakhrieh, A., Lins, G., Dinkelacker, F., Hammer, T., Leipertz, A., and Branston, D. W., "The Influence of Pressure on the Control of Premixed Turbulent Flames Using an Electric Field," *Combustion and Flame*, Vol. 143, No. 3, 2005, pp. 313–322.
doi:10.1016/j.combustflame.2005.06.009
- [14] Prikhod'ko, N. G., "Influence of the Electric Field on the Soot Formation in the Flame at a Low Pressure," *Journal of Engineering Physics and Thermophysics*, Vol. 83, No. 1, March 2010, pp. 154–161.
- [15] Saito, M., Arai, T., and Arai, M., "Control of Soot Emitted from Acetylene Diffusion Flames by Applying an Electric Field," *Combustion and Flame*, Vol. 119, No. 3, Nov. 1999, pp. 356–366.
doi:10.1016/S0010-2180(99)00065-6
- [16] Marcum, S. D., and Ganguly, B. N., "Electric-Field-Induced Flame Speed Modification," *Combustion and Flame*, Vol. 143, Nos. 1–2, 2005, pp. 27–36.
doi:10.1016/j.combustflame.2005.04.008
- [17] Altendorfer, F., Kuhl, J., Zigan, L., and Leipertz, A., "Study of the Influence of Electric Fields on Flames Using Planar LIF and PIV Techniques," *Proceedings of the Combustion Institute*, Vol. 33, No. 2, 2011, pp. 3195–3201.
- [18] Van Den Boom, J. D. B. J., Konnov, A. A., Verhasselt, A. M. H. H., Kornilov, V. N., De Goey, L. P. H., and Nijmeijer, H., "The Effect of a DC Electric Field on the Laminar Burning Velocity of Premixed Methane/Air Flames," *Proceedings of the Combustion Institute*, Vol. 32, No. 1, 2009, pp. 1237–1244.
- [19] De Goey, L. P. H., Van Oijen, J. A., Kornilov, V. N., and Ten Thije Boonkkamp, J. H. M., "Propagation, Dynamics and Control of Laminar Premixed Flames," *Proceedings of the Combustion Institute*, Vol. 33, No. 1, 2011, pp. 863–886.
- [20] Wisman, D. L., Marcum, S. D., and Ganguly, B. N., "Electrical Control of the Thermodiffusive Instability in Premixed Propane-Air Flames," *Combustion and Flame*, Vol. 151, No. 4, 2007, pp. 639–648.
doi:10.1016/j.combustflame.2007.06.021
- [21] Wisman, D. L., Marcum, S. D., and Ganguly, B. N., "Electric-Field-Induced Dissociative Recombination at the Base of Premixed Hydrocarbon/Air Flames," *43rd Joint Propulsion Conference & Exhibit*, AIAA Paper 2007-5672, July 2007.
- [22] Wisman, D. L., Ganguly, B. N., and Marcum, S. D., "Importance of Electrode Location on Flames Modified by Low Applied Electric Fields," *46th AIAA Aerospace Sciences Meeting and Exhibit*, AIAA Paper 2008-1397, Jan. 2008.
- [23] Payne, K. G., and Weinberg, F. J., "A Preliminary Investigation of Field-Induced Ion Movement in Flame Gases and Its Applications," *Proceedings of the Royal Society*, Vol. 250, No. 1262, March 1959, pp. 316–336.
- [24] Lawton, J., and Weinberg, F. J., "Maximum Ion Currents from Flames and the Maximum Practical Effects of Applied Electric Fields," *Proceedings of the Royal Society*, Vol. 277, No. 1371, Feb. 1964, pp. 468–497.
- [25] Xu, K. G., "Plasma Sheath Behavior and Ionic Wind Effect in Electric Field Modified Flames," *Combustion and Flame*, Vol. 161, No. 6, 2014, pp. 1678–1686.
doi:10.1016/j.combustflame.2013.12.008
- [26] Riemann, K.-U., "The Bohm Criterion and Sheath Formation," *Journal of Physics D: Applied Physics*, Vol. 24, No. 4, 1991, pp. 493–518.
doi:10.1088/0022-3727/24/4/001
- [27] Baglin, V., Bozhko, Y., Gröbner, O., Henrist, B., Hilleret, N., Scheuerlein, C., and Taborelli, M., "The Secondary Electron Yield of Technical Material and Its Variation with Surface Treatments," *Proceedings of EPAC 2000*, European Organization for Nuclear Research, Geneva, Switzerland, 2000, pp. 217–221.
- [28] Hayhurst, A. N., Goodings, J. M., and Taylor, S. G., "The Effects of Applying Electric Fields on the Mass Spectrometric Sampling of Positive and Negative Ions from a Flame at Atmospheric Pressure," *Combustion and Flame*, Vol. 161, No. 12, 2014, pp. 3249–3262.
doi:10.1016/j.combustflame.2014.06.012
- [29] Chen, Q., Yan, L., Zhang, H., and Li, G., "Electrical Characteristics, Electrode Sheath and Contamination Layer Behavior of a Meso-Scale Premixed Methane–Air Flame Under AC/DC Electric Fields," *Plasma Science and Technology*, Vol. 18, No. 5, 2016, pp. 569–576.
- [30] Jacobs, S. V., and Xu, K. G., "Examination of Ionic Wind and Cathode Sheath Effects in an E-Field Premixed Flame with Ion Density Measurements," *Physics of Plasmas*, Vol. 23, No. 4, 2016, Paper 43504.
doi:10.1063/1.4945614
- [31] Gan, Y., Wang, M., Luo, Y., Chen, X., and Xu, J., "Effects of Direct-Current Electric Fields on Flame Shape and Combustion Characteristics of Ethanol in Small Scale," *Advances in Mechanical Engineering*, Vol. 8, No. 1, 2016, pp. 1–14.
doi:10.1177/1687814015624846
- [32] Kamani, S., and Dunn-Rankin, D., "Detailed Characterization of DC Electric Field Effects on Small Non-Premixed Flames," *Combustion and Flame*, Vol. 162, No. 7, 2015, pp. 2865–2872.
doi:10.1016/j.combustflame.2015.03.019
- [33] Goodings, J. M., Bohme, D. K., and Ng, C.-W., "Detailed Ion Chemistry in Methane–Oxygen Flames. I. Positive Ions," *Combustion and Flame*, Vol. 36, Sept. 1979, pp. 27–43.
doi:10.1016/0010-2180(79)90044-0
- [34] Prager, J., Riedel, U., and Warnatz, J., "Modeling Ion Chemistry and Charged Species Diffusion in Lean Methane–Oxygen Flames," *Proceedings of the Combustion Institute*, Vol. 31, No. 1, 2007, pp. 1129–1137.
- [35] Schmidt, J., Kostka, S., Roy, S., Gord, J., and Ganguly, B., "kHz-Rate Particle-Image Velocimetry of Induced Instability in Premixed Propane/Air Flame by Millisecond Pulsed Current-Voltage," *Combustion and Flame*, Vol. 160, No. 2, 2013, pp. 276–284.
doi:10.1016/j.combustflame.2012.10.013
- [36] Ganguly, B. N., and Schmidt, J. B., "Pulsed Current-Voltage-Induced Perturbations of a Premixed Propane/Air Flame," *Journal of Combustion*, Vol. 2011, 2011, Paper 751651.
- [37] Kuhl, J., Jovicic, G., Zigan, L., and Leipertz, A., "Transient Electric Field Response of Laminar Premixed Flames," *Proceedings of the Combustion Institute*, Vol. 34, No. 2, 2013, pp. 3303–3310.
- [38] Altendorfer, F., Beyrau, F., Leipertz, A., Hammer, T., Most, D., Lins, G., and Branston, D. W., "Technical Feasibility of Electric Field Control for Turbulent Premixed Flames," *Chemical Engineering & Technology*, Vol. 33, No. 4, 2010, pp. 647–653.
- [39] Smy, P., "The Use of Langmuir Probes in the Study of High Pressure Plasmas," *Advances in Physics*, Vol. 25, No. 5, 1976, pp. 517–553.
doi:10.1080/00018737600101442
- [40] Pederson, T., Brown, R. C., Pedersen, T., and Brown, R. C., "Simulation of Electric Field Effects in Premixed Methane Flames," *Combustion and Flame*, Vol. 94, No. 4, 1993, pp. 433–448.
doi:10.1016/0010-2180(93)90125-M